

2024-01-15

Giant offshore pumice deposit records a shallow marine explosive eruption of ancestral Santorini

Druitt, T

<https://pearl.plymouth.ac.uk/handle/10026.1/21665>

10.1038/s43247-023-01171-z

Communications Earth & Environment

Nature Research

All content in PEARL is protected by copyright law. Author manuscripts are made available in accordance with publisher policies. Please cite only the published version using the details provided on the item record or document. In the absence of an open licence (e.g. Creative Commons), permissions for further reuse of content should be sought from the publisher or author.

Giant offshore pumice deposit records a shallow marine explosive eruption of ancestral Santorini

Tim Druitt¹, Steffen Kutterolf², Thomas A. Ronge³, Christian Hübscher⁴, Paraskevi Nomikou⁵, Jonas Preine⁴, Ralf Gertisser⁶, Jens Karstens², Jörg Keller⁷, Olga Koukousioura⁸, Michael Manga⁹, Abigail Metcalfe¹, Molly McCanta¹⁰, Iona McIntosh¹¹, Katharina Pank², Adam Woodhouse¹², Sarah Beethe¹³, Carole Berthod¹⁴, Shun Chiyonobu¹⁵, Hehe Chen¹⁶, Acacia Clark¹⁷, Susan DeBari¹⁸, Raymond Johnston¹⁹, Ally Peccia²⁰, Yuzuru Yamamoto²¹, Alexis Bernard²², Tatiana Fernandez Perez²³, Christopher Jones²⁴, Kumar Batuk Joshi²⁵, Günther Kletetschka²⁶, Xiaohui Li²⁷, Antony Morris²⁸, Paraskevi Polymenakou²⁹, Masako Tominaga³⁰, Dimitrios Papanikolaou⁵.

¹Laboratoire Magmas et Volcans, Université Clermont Auvergne, F-63000 Clermont-Ferrand, France

²GEOMAR Helmholtz Centre for Ocean Research Kiel, Wischhofstrasse 1-3, D-24148 Kiel, Germany

³International Ocean Discovery Program, Texas A&M University, College Station TX 77845, USA

⁴Institute of Geophysics, University of Hamburg, Bundesstrasse 55, D-20146 Hamburg, Germany

⁵Department of Geology and Geoenvironment, National and Kapodistrian University of Athens, 15784 Athens, Greece

⁶School of Geography, Geology and the Environment, Keele University, Staffordshire ST5 5BG, UK

⁷Mineralogie und Petrologie, Albert-Ludwigs-Universität, Freiburg, Germany

⁸School of Geology, Aristotle University of Thessaloniki, 54124 Thessaloniki, Greece

⁹Department of Earth and Planetary Science, University of California, Berkeley, CA 94720, USA

¹⁰Department of Earth and Planetary Sciences, University of Tennessee, Knoxville TN 37996-1526, USA

¹¹Japan Agency for Marine-Earth Science and Technology, 2-15 Natsushima-cho, Yokosuka Kanagawa 237-0061, Japan

¹²Institute for Geophysics, University of Texas, J.J. Pickle Research Campus, Bldg. 196, Austin TX 78758, USA

¹³College of Earth, Ocean, and Atmospheric Sciences, Oregon State University, Corvallis OR 97333, USA

¹⁴Institut De Physique Du Globe De Paris, Centre National de la Recherche Scientifique (CNRS), 75005 Paris, France

¹⁵Faculty of International Resource Sciences, Akita University, Akita, Akita Prefecture 0108502, Japan

¹⁶School of Ocean Sciences, China University of Geosciences, 100083 Haidan District, Beijing, China

¹⁷School of Natural Sciences/CODES, University of Tasmania, Hobart 7005, Australia

¹⁸Geology Department, Western Washington University, Bellingham WA 98225, USA

¹⁹School of Geosciences, University of South Florida, Tampa FL 33620, USA

²⁰Lamont-Doherty Earth Observatory, Columbia University, Palisades NY 10964, USA

²¹Graduate School of Science, Kobe University, 1-1 Rokkodai-cho, Nada-ku, Kobe, Hyogo 657-8501, Japan

²²Laboratoire des Fluides Complexes et leurs Réservoirs, Université de Pau et des Pays de l'Adour, F-64000 Pau, France

²³Department of Geology, Kent State University, 221 McGilvrey Hall, 325 S Lincoln Street, Kent OH 44242, USA

²⁴Department of Earth and Planetary Sciences, University of California, Riverside CA 92506, USA

²⁵Solid Earth Research Group, National Centre for Earth Science Studies, Thiruvananthapuram, Kerala 695011, India

²⁶Geophysical Institute, University of Alaska Fairbanks, 324 Reichard Building, Fairbanks Alaska 99709, USA

²⁷Key Laboratory of Submarine Geoscience and Prospecting Techniques, Ocean University of China, Qingdao, China

²⁸School of Geography, Earth and Environmental Sciences, Plymouth University, Drake Circus, Plymouth PL4 8AA, UK

²⁹Institute of Marine Biology, Biotechnology and Aquaculture, Hellenic Centre for Marine Research, Heraklion, Greece

³⁰Department of Geology and Geophysics, Woods Hole Oceanographic Institution, Woods Hole MA 02543, USA

49 **Abstract**

50 **Large explosive volcanic eruptions from island arcs pour pyroclastic currents into marine basins,**
51 **impacting ecosystems and generating tsunamis that threaten coastal communities. Risk**
52 **assessments require robust records of such highly hazardous events, which is challenging as most**
53 **of the products lie buried under the sea. Here we report the discovery by IODP Expedition 398 of a**
54 **giant rhyolitic pumice deposit emplaced 520 ± 10 ky ago at water depths of 200 to 1000 m during a**
55 **high-intensity, shallow submarine eruption of ancestral Santorini Volcano. Pyroclastic currents**
56 **discharged into the sea transformed into water-saturated gravity flows, forming a $>89 \pm 8$ km³**
57 **volcaniclastic megaturbidite up to 150 m thick in the surrounding marine basins, while breaching of**
58 **the sea surface by the eruption column laid down veneers of ignimbrite on three islands. The**
59 **eruption is one of the largest recorded on the South Aegean Volcanic Arc, and highlights the**
60 **hazards associated with submarine explosive eruptions.**

61

62

63 **Introduction**

64 The processes and impacts of submarine explosive eruptions are poorly understood in comparison to
65 their terrestrial equivalents¹⁻⁵. However, submarine calderas are common on island arcs^{6,7} and
66 shallow submarine eruptions can be very violent as shown by that of Hunga Tonga–Hunga Ha’apai
67 Volcano in 2022⁸⁻¹⁰. Pyroclastic currents from such eruptions pour into the sea, entraining water and
68 transforming into water-saturated gravity flows¹¹⁻¹⁴. Although the resulting deposits can be studied in
69 ancient successions, those within marine sediments around modern island volcanoes are difficult to
70 access except by deep drilling.

71 The South Aegean Volcanic Arc lies in the heart of Europe, and its submarine volcanoes are
72 potentially a major hazard^{15,16}. While the eruptive history of the arc has been investigated through
73 onland mapping and marine tephrachronology¹⁷⁻¹⁹, the record of submarine volcanism has only been
74 broadly constrained by offshore seismic imagery²⁰⁻²³. In 2022-23, IODP Expedition 398 drilled the
75 marine rifts of the central island arc to depths of up to 900 m below the seafloor in order to ground-
76 truth the seismic stratigraphy, to use the basin sediments as time capsules to recover a complete
77 record of Neogene-Quaternary volcanism, and to seek deposits from past submarine eruptions.

78 The twelve drill sites lie in and around the Christiana-Santorini-Kolumbo Volcanic Field (CSKVF),
79 which hosts Santorini caldera. The CSKVF is situated within a 100-km-long, NE-SW rift system that
80 cuts across the volcanic arc and consists of three basins (Anhydros, Amorgos, Anafi) containing up to
81 1400 m of sediments and volcanics above continental basement²¹⁻²⁴(Fig. 1). To the south, these
82 basins cut an earlier E-W-trending rift that forms the Christiana Basin²⁵⁻²⁷. Christiana Volcano has

83 been extinct since $\sim 1.6 \text{ Ma}^{23}$, and its eroded remnants make up the small islands of Christiani and
84 Askani. Santorini has been active since at least 650 ka, and it last erupted in 1950 CE. Its activity can
85 be grouped geochemically into old (>650 to 550 ka; 'Early Centres of Akrotiri') and young (530 ka to
86 present day) periods^{17,28}. At least twelve Plinian eruptions have occurred at Santorini since 360 ka,
87 the youngest of which was the $\sim 1600 \text{ BCE}$ Minoan eruption: an iconic event in volcanology and
88 archaeology. It was unknown until the present study that major explosive activity took place at the
89 CSKVF before 360 ka¹⁷. Kolumbo Volcano and its chain of submarine cones are located NE of
90 Santorini²⁴. The 1650 CE submarine eruption of Kolumbo killed about 70 people on Santorini^{29,30}.

91 Deep drilling provided us with a unique opportunity to generate a full eruptive time series of
92 the CSKVF, completing a well-studied but incomplete onland story. Additional motivation was
93 provided by a caldera unrest period in 2011-12³¹, and the presence of two shallow magma reservoirs
94 (Santorini and Kolumbo^{32,33}), in a region visited by two million tourists per year. The discovery of the
95 submarine pumice deposit that is the subject of this paper exploited a unique combination of IODP
96 deep drilling, large multidisciplinary shipboard datasets, laboratory analysis, and a dense network of
97 marine seismic profiles.

98

99 **Results**

100 **The submarine eruptive products**

101 The newly discovered deposit, which we call the Archaeos Tuff, was sampled at seven drill sites
102 around Santorini, with recoveries ranging from <1 to 88 % (Fig. 1; Table 1). It was thickest in cores
103 from the Christiana Basin (65 m, Site U1591; >46 m, Site 1598) and immediately north of Santorini
104 (75 m, Site U1593), of intermediate thickness in the Anafi Basin (50 m, Site U1592; 32 m, Site U1599),
105 and thinnest at the distal end of the Anhydros Basin (8 m, Site U1589). A thin layer occurs atop the
106 horst separating the Anhydros and Anafi Basins (6 m, Site U1600) (Fig. 2a).

107 The deposit is composed of massive to diffusely bedded pumice and ash with lesser lithic
108 components (Fig. 3a-e; Supplementary Table 1). Clast-supported pumice lapilli dominate at sites close
109 to Santorini (U1591, U1598, U1593), whereas ash dominates at the most distal site (U1589)(Fig. 3a-e).
110 Grain-size analysis of the deposit is complicated by the disturbance effects of drilling and core
111 recovery³⁴ (see Methods); however samples judged to be least affected by core disturbance have
112 median diameters of -1.9 to 3.3 phi, Inman sorting coefficients³⁵ of 1.4 to 2.9 phi, <20 % of sub-63 μm
113 ash, and are better sorted and poorer in fine ash than subaerial ignimbrites³⁶ (Fig. 3f-g). With 30-98
114 wt% of ash (<2 mm) components, the deposits are lapilli tuffs and tuffs (in what follows we use 'tuff'
115 for brevity). Most samples are unimodal, but some distal samples (U1589) are bimodal, with coexisting
116 modes of pumice lapilli (2-4 mm) and ash (63-125 μm)(Supplementary Table 2). The deposit is rich in

117 pumice, which comprises almost all of the lapilli (>2 mm) size fraction and dominates the ash fractions.
118 The largest pumice clasts are typically less than a few cm in size and decrease with distance from
119 Santorini (Fig 2b). Cuts through pumices larger than the drill core diameter (6.2 cm) are very rare. The
120 largest lithic clasts are smaller than pumices at a given site and also decrease in maximum size away
121 from Santorini (Fig. 2b). Lithic lapilli also occur concentrated in rare, cm-thick clast-supported layers
122 within the tuffs (Fig 3c). An abundance of lithic clasts larger than lapilli size can probably be ruled out
123 because they would have been partially recovered by the drilling.

124 Pumice clasts are variably angular to rounded. Vesicles comprise 75.9 ± 4.4 vol% of pumice
125 lapilli, with 63.5 ± 7.5 vol % being connected and 12.4 ± 3.8 vol% isolated (Supplementary Table 3),
126 and they range in shape from spherical to tubular. Chemical analyses of the 78 wt% SiO₂ high-silica
127 rhyolite glasses from 38 pumice samples from seven drill sites are mutually identical in terms of
128 major elements, trace elements and incompatible trace element ratios to within analytical
129 uncertainty (Fig. 4; Supplementary Table 4). They are compositionally distinct (e.g., higher Ba/Zr,
130 Ba/Y; lower Zr/Nb, Zr/Rb) from the products of Christiana, Kolumbo, other volcanic fields of the
131 island arc, and young (<530 ka) Santorini¹⁹, and are most similar to those of the old (>650-55 ka)
132 Akrotiri centres of Santorini (Fig. 4). Phenocrysts comprise a small percentage of the pumices and
133 include plagioclase, quartz, cummingtonite, augite, hypersthene, magnetite, ilmenite and zircon
134 (Supplementary Fig. 1, Tables 5 and 6). Lithic components are mainly lavas, although greenschists
135 (Fig. 3c), limestones and granitoids also occur. Bioclasts picked up from the sea bed are common.
136

137 **Biostratigraphic constraints on eruption age**

138 Foraminifer and calcareous nannofossil assemblages in sediment layers above the Archaeos Tuff
139 constrain the eruption age at 520 ± 10 ka (Fig. 2a; see Methods). We focus particularly on the upper
140 contact because the lower contact is erosive on some seismic profiles. The biostratigraphic datum for
141 510 ka lies within \pm a few metres of the upper contact at Sites U1591, U1593, U1599 and U1600,
142 suggesting an eruption age of \sim 510 ka. The occurrence of this datum immediately below the tuff at
143 Site U1589 could be due to post-eruptive remobilization of the ash-rich material down the basin.
144 Downward extrapolation of sedimentation rates towards the upper contact at Site U1591, using the
145 467 ka and 510 ka datums in the overlying sediments, gives 520 ± 10 ka the top of the tuff, the
146 uncertainty arising from the \pm 9.5 m depth imprecision on the one-per-core datum levels. The
147 occurrence of the 610 ka datum above the tuff at Site U1592 (Fig. 2a) is attributed to reworking
148 within an overlying mass flow deposit recognized by its sedimentary characteristics in the cores.
149

150 **Emplacement water depths**

151 The Archaeos Tuff was emplaced at water depths of several hundreds of metres, comparable to the
152 present-day basin bathymetry. Despite eustatic sea level having been ~50 m lower than the present
153 day at the time of the eruption³⁷, resulting in greater land exposure³⁸, the tuff is intercalated with
154 marine sediments such as oozes and was clearly emplaced under water. Benthic foraminifer
155 assemblages in sediments above and below the deposit constrain the local palaeobathymetry prior
156 to, or following, the eruption (see Methods). Palaeowater depths thus inferred are 200-700 m in the
157 Christiana Basin (Site U1591), 500-1000 m along the axis of the Anafi Basin (U1592), and 200-700 m
158 in the Anhydros Basin (U1589) and at the margin of the Anafi Basin (U1599) (Supplementary Table 7).

159

160 **Seismic stratigraphy and volume**

161 The deposit forms an acoustically chaotic to transparent layer on the seismic profiles that can be
162 traced through all the rift basins, ground-truthed by the core-seismic correlation and biostratigraphic
163 ages (Fig. 5; Supplementary Fig. 2). In the Christiana Basin this layer was previously interpreted as a
164 pyroclastic current deposit (ref 25; their seismic Layer III), or as the product of large-scale mass
165 wasting (ref 27; parts U4c and U4d of their seismic Unit U4), but our cores confirm a pyroclastic
166 origin. On a thickness map, the deposit reaches up to 150 m in the basin between Christiana and
167 Santorini as well as in the Anafi Basin (Fig. 5a). The basal contact is erosive in the Christiana Basin and
168 on the southeastern flank of Santorini, but conformable at other basin sites (Fig. 5b).

169 Integration of the thickness of the tuff across our pre-existing dense array of single channel
170 and multichannel seismic profiles^{21-23,27} yields an observed bulk volume of $89 \pm 8 \text{ km}^3$ using *in situ*
171 shipboard measurements of P-wave velocity (see Methods). This is the volume contained within the
172 area covered by our seismic network (Fig. 5a) and is a minimum estimate of the total volume. The ± 9
173 % uncertainty on the volume arises from that on the P-wave velocity ($1865 \pm 168 \text{ m s}^{-1}$).

174 Conversion of bulk to DRE (Dense Rock Equivalent) volumes of pyroclastic deposits commonly
175 makes simplified assumptions about the porosity of the uncompacted tuff. In the present study, a
176 unique set of high-resolution shipboard measurements allowed conversion to DRE using real *in situ*
177 data (see Methods). Shipboard density and pycnometry measurements on 72 core samples of the
178 Archaeos Tuff showed that DRE volume is on average 0.341 ± 0.009 times that of the uncompacted
179 volume (equivalent to a mean deposit porosity of $65.9 \pm 0.9 \%$), yielding an observed DRE volume of
180 $30 \pm 3 \text{ km}^3$.

181

182 **Onland correlatives**

183 Onland outcrops of a geochemically distinctive rhyolitic tuff occurring on Christiani, Santorini, and
184 Anafi islands (Fig. 1) studied and intercorrelated by Keller et al.^{39,40}, can now be attributed to the
185 Archaeos eruption (Supplementary Fig. 3 and Table 8). The outcrops are each a few metres or less in

186 thickness and are of limited extent, so their volume is negligible compared to that of the submarine
187 facies. They consist of poorly sorted (Inman sorting coefficients³⁵ of 3.9 to 4.2) lapilli tuffs with the
188 characteristics of subaerial ignimbrite (Fig. 3f,g; Supplementary Fig. 3 and Table 8). On Christiani
189 Island the deposit lies on Pleistocene lavas from Christiana Volcano, and on Santorini and Anafi it lies
190 on metamorphic basement. Maximum lithic clast sizes are ~4 cm on Anafi, ~10 cm on Santorini and
191 ~1 m on Christiani, the latter occurring as lithic breccia lenses within the ignimbrite. Correlation with
192 the submarine Archaeos Tuff is based on (1) chemically similar glasses and minerals (Supplementary
193 Tables 4-6), (2) the occurrence of cummingtonite, (3) common tubular pumices, and (4) similar lithic
194 assemblages including granitoids and greenschists. The occurrence of cummingtonite is notable;
195 other occurrences of amphibole in the CSKVF belong mostly to the calcic amphibole series (Early
196 Centres of Akrotiri, 1650 CE pumice of Kolumbo, some lavas of Christiana, and very rarely in the
197 Thera pyroclastics^{18,29}), although some Akrotiri tuffs contain cummingtonite coexisting with calcic
198 amphibole (Supplementary Fig. 1).

199

200 **Discussion**

201 **Eruption and emplacement**

202 We interpret the Archaeos Tuff as a volcanoclastic megaturbidite emplaced by a powerful shallow
203 submarine explosive eruption, the column from which collapsed mainly under water. Fountaining of
204 the column poured pyroclastic currents into the surrounding marine basins, where they transformed
205 into water-saturated gravity flows through entrainment of sea water. Breaching of the sea surface by
206 the eruption column also produced subaerial pyroclastic currents that laid down thin layers of
207 ignimbrite on nearby islands. The uniform melt chemistry, distinctive mineral assemblage, and lack of
208 observed depositional breaks favour a single volcanic event. The eruptive intensity must have been
209 very high to explain the >3000 km² geographic footprint of the submarine deposit and ignimbrite
210 veneers on islands up to 55 km apart. The high vesicularities of pumice lapilli show that magma
211 fragmentation was driven mainly by exsolution of magmatic gases, although components of
212 phreatomagmatic and quench fragmentation in contact with sea water cannot be excluded³⁰.

213 Submarine deposits from pyroclastic currents can be emplaced by a range of processes,
214 including hot, gas-supported gravity flows, water-saturated gravity flows, and fallout from
215 suspension plumes, pumice rafts and pyroclastic currents flowing across the sea ^{1,10-14,41-50}.
216 Emplacement of the submarine Archaeos Tuff by gravity flows is implied by its great thickness,
217 thickening into the rift basins, and locally erosional base^{10,12-14}. Fallout from the processes listed
218 above probably accompanied gravity flow emplacement, but cannot have been the dominant
219 emplacement mechanism because it would have produced a thinner, less channelized

220 deposit^{41,44,49,51}. Secondary remobilisation of syn-eruptive deposits, both on the sea floor and from
221 neighbouring islands, may have continued to generate gravity flows after the eruption.

222 The depositional temperature of the submarine tuff is hard to assess, but the lack of particle
223 sintering textures or any observed gas escape pipes probably rules out very hot emplacement from
224 gas-supported flows¹¹ at our drill sites. The moderate to good sorting of the deposit is more
225 consistent with transport in water-supported gravity flows since the higher density and viscosity of
226 water sorts particles of different sizes and densities more efficiently than gas^{30,41,49}. This probably
227 explains the better sorting and fines depletion of the submarine tuff compared to its onland
228 ignimbrite (Fig. 3f-g). Moreover, the maximum clast sizes of pumices and lithics in the submarine tuff
229 are calculated to be in approximate hydraulic equivalence in water if the connected pore space of the
230 pumices was waterlogged (see Methods), while the moderate to low rounding of the pumice lapilli
231 may be attributed to the lower energy of interparticle impacts in water-saturated gravity flows than
232 in gas-supported ones¹²⁻¹⁴. Our observations are consistent with studies of ancient submarine tuffs<sup>10-
233 14,42-46</sup>, and experiments of flowing hot ash into water⁴⁷, showing that hot pyroclastic currents
234 entering the sea (either from submarine or subaerial vents) rapidly entrain water and transform into
235 water-saturated turbidity currents, and that submarine deposits from hot gas-particle flows are
236 limited to near-shoreline environments^{11,48}. We envisage a flux of turbidity currents and granular
237 slurries sustained over many hours or days to generate the Archaeos megaturbidite.

238 Although the evidence favours relatively cold emplacement of the submarine tuff at our drill
239 sites, the abundance of highly vesicular pumice suggests that the initial pyroclastic currents entered
240 the water column at high temperature. While cold pumice floats in water, hot pumices sink and are
241 incorporated into gravity flows because they saturate with water drawn into interconnected vesicles
242 as the magmatic gases thermally contract and change phase^{52,53}. Pumices larger than a few cm are
243 probably scarce because large hot pumices in water take longer to saturate than small ones; they
244 first float to the sea surface forming a pumice raft before later saturating and sinking^{44,52,53}. Any
245 pumice rafts from the eruption must have been dispersed by surface currents⁵⁰, because we have not
246 observed accumulations of large pumices at the top of the tuff at our drill sites⁴⁹. Alternatively,
247 magma fragmentation during the high-intensity eruption may have been sufficiently efficient for
248 pumices larger than lapilli size not to have been produced in any great abundance. Lithic clasts larger
249 than a few cm in size probably fell out of the gravity flows close to source, leaving a sustained flux of
250 turbidity currents and slurries rich in pumice, small lithics and ash to spread out across the sea
251 floor^{13,47}.

252 Establishing whether a submarine volcanoclastic deposit was erupted from submarine or
253 subaerial vents is difficult⁴⁹, and a combination is of course possible around a large collapsing caldera
254 in a marine environment. Although we cannot completely exclude island vents, the collective

255 evidence favours eruption of the Archaeos Tuff from shallow submarine vents. By ‘shallow’ in this
256 context, we mean less than about ~1 km water depth where magmatic fragmentation and formation
257 of highly vesicular pumice is possible^{1,4,7}. First, apart from Christiana and the basement precursor
258 island of Santorini¹⁷, little of the CSKVF existed above sea level 520 ky ago. Products older than 520
259 ka on Santorini are submarine tuffs, subsequently tectonically uplifted. Given that sea level 520 ky
260 ago was only ~50 m lower than today³⁷, the Archaeos eruptive vents were probably under water.
261 Secondly, thick submarine, eruption-fed megaturbidites rich in well sorted pumice and ash are typical
262 of ‘Neptunian’ explosive eruptions from shallow submarine vents¹³. The pumice-lapilli-rich facies in
263 the Christiana Basin (Sites U1591 and 1598; Fig 3a-c) is particularly distinctive in this respect. Thirdly,
264 the great thickness of the Archaeos megaturbidite compared to its onland ignimbrite facies is
265 notable. It contrasts in this respect with Santorini tuffs like the Minoan, which produced thick onland
266 sequences⁵⁴. High-velocity gas-particle jets discharged in shallow submarine eruptions entrain sea
267 water, which can cause the jet to collapse as gravity flows before reaching the surface²⁻⁴. This
268 confines most of the pyroclastic products to the submarine realm, depositing little on nearby islands.
269 For a mass discharge rate typical of large ignimbrite eruptions ($\sim 10^9 \text{ kg s}^{-1}$)⁵⁵, the minimum water
270 depth for jet collapse is $\sim 200 \text{ m}$ ⁴. Taken together, the features of the Archaeos Tuff are most
271 consistent with the eruption of pyroclastic currents from shallow submarine vents.

272 The presence of poorly sorted ignimbrite on Christiana, Santorini and Anafi islands shows,
273 however, that the upper part of the eruption column breached the sea surface, sending gas-
274 supported pyroclastic currents across the sea. This may have occurred at periods of peak discharge,
275 or later in the eruption once the vent had shallowed^{2,29}. The mechanisms by which pyroclastic
276 currents travel across water and lay down ignimbrite on neighbouring islands have been widely
277 discussed⁵⁶⁻⁵⁸. While we cannot exclude the existence of Middle Pleistocene islands between
278 Christiani and Santorini (where no drill sites are present), our pre-eruption palaeobathymetry data at
279 Site U1599 (200-700 m; Supplementary Table 7) rules out a land bridge extending 30 km eastwards
280 to Anafi. Possibly the subaerial pyroclastic currents were density-stratified and their upper, less
281 dense parts travelled over the sea⁵⁹⁻⁶², or they flowed across pumice rafts during the latter stages of
282 the eruption.

283

284 **Eruption source**

285 Large-volume pyroclastic currents discharge during caldera-forming eruptions from long-lived
286 polygenetic volcanic complexes. The Archaeos eruption products are compositionally distinct from
287 those of Christiana, Kolumbo, and young (<530 ka) Santorini, and are most similar to those of the old
288 Akrotiri centres (Fig. 4a-c). They also resemble some Akrotiri tuffs in containing cummingtonite. They
289 are not, however, chemically identical to Akrotiri, showing that they represent a similar, but distinct,

290 batch of rhyolitic magma. The Akrotiri products are mainly submarine rhyolitic tuffs that have
291 subsequently been uplifted to ~100 m above present day sea level¹⁷. We infer that the Archaeos
292 eruption culminated the development of the submarine Akrotiri complex, and this further supports
293 our interpretation that the eruption took place from a submarine vent complex. The location of its
294 source caldera is, however, unclear. The caldera may lie buried beneath present-day Santorini,
295 consistent with the broadly symmetrical distribution of the submarine tuff around Santorini.
296 Alternatively, it may have lain in the densely faulted basin between Santorini and Christiana (Fig. 1),
297 which might explain the tuff thickness of up to 150 m in this basin and why the onland ignimbrite is
298 coarsest, with prominent lithic breccia lenses, on Christiani Island. Note that eruption-fed flows
299 sourced between Santorini and Christiana would have had free access into the Anhydros and Anafi
300 Basins because much of subaerial Santorini did not exist at that time¹⁷. Further seismic studies will be
301 required to precisely locate the source caldera.

302 The 520 ± 10 ka age of the Archaeos eruption lies near the transition between the Akrotiri
303 (>650 - 550 ka) and younger Santorini (<530 ka) periods, which were characterized by geochemically
304 different suites of magmas (Fig. 4a-c). We infer that crustal stress changes following the Archaeos
305 eruption were sufficiently large to trigger the tapping of new magma batches from storage zones in
306 the crust and mantle.

307

308 **Implications for the arc**

309 The observed 89 ± 8 km³ volume (30 ± 3 km³ DRE) of the Archaeos Tuff makes it the largest
310 pyroclastic current deposit of the CSKVF. It is six times bigger than the pyroclastic current deposit
311 from the Minoan eruption, recently re-evaluated at 14.8 ± 0.8 km³ uncompacted volume⁵⁴. While the
312 Minoan offshore deposits at Sites U1591 and U1598 are only ~2 m thick, those of Archaeos are thirty
313 times thicker. The drilling rules out the formation of any submarine tuffs larger than Archaeos in the
314 history of the CSKVF, since it traversed the sedimentary fills of the Anhydros and Anafi Basins to
315 Alpine basement.

316 Estimating the total volume of products from explosive eruptions is challenging⁶³⁻⁶⁶. Owing to
317 our dense seismic network (ground-truthed by drilling) and shipboard core P-wave velocity and
318 density measurements, the volume of the submarine tuff within the zone of study is well
319 constrained. However, 89 ± 8 km³ is a minimum estimate of the total eruption volume because it
320 does not take into account (1) distal flow deposits outside of the study area (including any that
321 spilled over into the Cretan basin; Fig. 1), (2) water-suspended and airborne co-ignimbrite ash
322 transported out of the study area, (3) pumice rafts, and (4) intra-caldera tuff. The distal flow volume
323 (1) might be estimated crudely from Fig. 5c, which shows a plot of log (thickness) versus cumulative
324 area. Like subaerial pyroclastic current deposits^{63,64}, the Archaeos data form an approximately linear

325 trend which, when extrapolated to 1 m thickness, yields a volume of $\sim 105 \text{ km}^3$. The other volume
326 components (2 to 4) could significantly increase this, but their contributions cannot be quantified
327 since the record of Middle Pleistocene ash layers in the eastern Mediterranean is sparse^{19,67}, the sizes
328 of any pumice rafts are unconstrained, and the location and size of the source caldera is unknown. It
329 is likely that our minimum volume estimate significantly underestimates the total volume of the
330 Archaeos eruption. Until now the largest eruption of the South Aegean Volcanic Arc has been
331 considered to be the 161 ka Kos Plateau Tuff (KPT)⁶⁸. The DRE volume of the KPT has been estimated
332 as 71 km^3 DRE (including co-ignimbrite ash) using a larger, less well constrained DRE-to-bulk
333 conversion factor¹⁹, but using our factor (which is similar to that determined for the Minoan
334 products⁵⁴) decreases it to 42 km^3 . Given the uncertainties, the Archaeos and Kos Plateau eruptions
335 may have been of similar magnitude.

336 We have documented both the offshore and onshore deposits from a large, shallow submarine
337 explosive eruption, well constrained by volume, age, bathymetric, field and geochemical data, the
338 pyroclastic currents from which were more than ten times larger in volume than the $\sim 6 \text{ km}^3$ of Hunga
339 Tonga–Hunga Ha’apai Volcano in 2022⁹. The findings change our current understanding of the South
340 Aegean Volcanic Arc, revealing a greater capacity for highly hazardous submarine volcanism than
341 previously known. They extend the explosive eruptive history of the CSKVF back in time, reveal a
342 submarine pyroclastic deposit possibly comparable in size to the Kos Plateau Tuff, and imply the
343 existence of a large buried submarine caldera on which the modern volcanic field is founded. The
344 under-representation of the Archaeos Tuff in the subaerial geological record highlights the
345 importance of deep drilling in unravelling the full secrets of island arcs, particularly in densely
346 populated regions like the Mediterranean.

347

348

349 **Data and methods**

350 **Deep-sea drilling**

351 IODP Expedition 398 took place on the *JOIDES Resolution* over two months, and drilled at twelve sites
352 in and around the Christiana-Santorini-Kolumbo Volcanic Field (CSKVF). Details of the seven sites at
353 which the Archaeos Tuff was recovered are given in Table 1. Two to three holes (A,B,C) were drilled
354 $\sim 50 \text{ m}$ apart at each site, and the Archaeos Tuff was intersected in one or more of these holes using
355 either Advanced Piston Coring (9.5 m stroke) or Half-Length Advanced Piston Coring (4.7 m stroke).
356 The core diameters are 6.2 cm. Uncertainties arose in the depth of the top and base of the deposit at
357 some sites due to imperfect core recovery; however subsequent core-seismic correlation allowed
358 these to be precisely determined (Table 1). The standard array of shipboard physical properties

359 measurements were made on the cores (<https://iodp.tamu.edu/labs/index.html>). The cores were
 360 logged and described using the standard pyroclastic terminology⁶⁹, taking into account artefacts of
 361 drilling and core recovery such as sediment mixing, shear-induced uparching, brecciation, biscuiting
 362 and ash liquefaction³⁴. Samples of pumice lapilli and ash were collected from the cores for chemical
 363 and mineralogical analysis. Bulk sediment samples were taken from the core catcher of every core
 364 for micropalaeontological analysis and determination of biostratigraphic ages and palaeowater
 365 depths.

366

367 **Table 1. Details of sites containing the Archaeos Tuff**

Site	Water depth (mbsl)	Penetration (mbsf)	Holes with Archaeos Tuff	Top of Archaeos Tuff (mbsf)*	Base of Archaeos Tuff (mbsf)*	Thickness of Archaeos Tuff (m)*	% recovery of Archaeos Tuff interval
U1589	484	622	A, B	300	308	8	88
U1591	514	903	A, B	65	130	65	19
U1592	693	528	B	350	400	50	<1
U1593	404	193	A, B	115	190	75	50
U1598	521	99	A, B	61	>107	>46	34
U1599	592	698	A, B	150	182	32	71
U1600	326	189	A, B	37	43	6	58

368 *Determined by coring and refined from core-seismic correlation in cases of poor core recovery. mbsf : metres below sea
 369 floor

370

371 Bathymetry

372 The digital elevation model (DEM; Fig. 1) was produced by merging satellite-derived Advanced
 373 Spaceborne Thermal Emission and Reflection Radiometer (ASTER) data, a community-sourced DEM
 374 from the European Marine Observation and Data Network (EMODnet), data acquired on board the
 375 *R/V Aegaeo* during the GEOWARN project, and data from the *R/V Marcus G. Langseth* during the
 376 PROTEUS seismic tomography project^{15,24,70}. The swath dataset has a lateral resolution of 20 m. It was
 377 collected with the SEABEAM 2120 20 kHz swath system onboard *R/V Aegaeo* and with the Simrad
 378 Kongsberg EM122 12 kHz multibeam echo sounder on the *R/V Marcus G. Langseth*^{24,70}.

379

380

381 Onland field work

382 We visited the onland occurrences of the Archaeos Tuff on Christiani, and Santorini and Anafi
 383 following earlier studies^{39,71,72}. We restudied the outcrops, and collected new pumice samples for
 384 chemical analysis using the same analytical conditions as for the core samples. Keller et al.³⁹ inter-
 385 correlated the three occurrences and interpreted the deposit as the product of a major ignimbrite
 386 event early in the history of the Santorini volcano group. This interpretation is confirmed by our new
 387 findings.

388

389 **Chemical analysis**

390 Glasses and phenocrysts in pumice lapilli from the onland and submarine facies of the Archaeos Tuff
391 were analysed for correlation purposes. We crushed 2-3 pumice lapilli from each proximal or medial
392 site, but used bulk ash samples from the more distal sites. We sieved the material into grain size
393 fractions with deionized water, embedding the 63–250 µm fraction with epoxy resin into 12 pre-
394 drilled holes in acrylic mounts and polishing to facilitate measurements with the electron microprobe
395 (EMP) and the Laser Ablation Inductively Coupled Plasma Mass Spectrometer (LA-ICP-MS). We also
396 mounted representative phenocryst phases in epoxy.

397 Major and minor elements of glasses were analysed using a JEOL JXA 8200 wavelength
398 dispersive EMP at GEOMAR, Kiel, using an accelerating voltage of 15 kV, a beam current of 6 nA, and
399 a 10 µm diameter electron beam to minimize sodium loss. Oxide concentrations were determined
400 using the ZAF correction method. Accuracy was monitored by two measurements each on Lipari
401 obsidian⁷³ and Smithsonian basaltic standard VGA99⁷⁴ after every 60 analyses. All analyses with totals
402 of >90 wt% were renormalized to 100% to eliminate the effects of variable post-depositional
403 hydration and minor deviations in focusing of the electron beam. Major and minor element
404 compositions of amphibole phenocrysts were analyzed by EMP at the University of Tennessee using a
405 1 µm spot size with a probe current of 30 nA and an accelerating voltage of 15 kV.

406 Trace element contents of glass shards were analyzed by LA-ICP-MS in two laboratories: the
407 Laboratory of Magmatism and Volcanism in Clermont-Ferrand, France, and at the Academia Sinica in
408 Taipei, Taiwan. Both laboratories used 193 nm Excimer lasers with 24-30 µm beam sizes connected
409 to Agilent 7500 or 7900 ICP-MS instruments. Background was counted for between 20 and 45 s, and
410 samples for between 75 and 100 s. The internal standard was ⁴⁴Ca, with CaO contents determined by
411 EMP on the same glass shard. The external standard was NIST 612 and the secondary standard was
412 BCR. The GLITTER software was used to reduce the data and calibrate with standards to obtain trace
413 element concentrations, The limit of detection was <100 ppb for most trace elements and ~10 ppb
414 for Rare Earth Elements. The analytical precision was better than 10% for most trace elements. One
415 sample of the Archaeos Tuff was analyzed in both laboratories and the trace element concentrations
416 and ratios were found to be the same within analytical uncertainty.

417 **Textural and grain size measurements**

418 Cores from IODP Expedition 398 rich in pumice and ash such at the Archaeos Tuff were subject to
419 disturbance effects during coring and recovery³⁴. In particular, the ash may in some cases liquefied,
420 allowing some of the ash components to decant to the top of the core during post-recovery re-
421 sedimentation. Consequently many cores had tops enriched in segregated ash. Fall-in of ash into the

422 drill hole between cores also occurred, resulting in an ash-rich layer at the top of some cores. For
423 these reasons we avoid presenting logs of the cores, which would be misleading. Granulometric
424 analysis is also challenging due to fines segregation within the cores. We addressed this problem by
425 identifying levels in the cores that were little effected by liquefaction: (1) tightly interlocking lapilli
426 and ash which had appeared to have escaped the effect, or (2) intervals of the cores lacking any
427 visible grading in fines content. Twenty such samples (masses 8 to 82 g) covering the range of
428 lithologies were sieved at 1 phi intervals from -3 to 4 phi.

429

430 **Connected and isolated vesicularities of pumice lapilli**

431 The connected and isolated vesicularities of twenty representative pumice lapilli in the 1-3 cm size
432 range, collected from the Archaeos Tuff at Sites U1591 and U1598, were measured at the Laboratory
433 of Magmatism and Volcanism in Clermont-Ferrand, France. The lapilli were washed, dried and
434 weighed. The envelope volumes were then measured using a Micromeritics Geopyc 1360 Envelope
435 and T.A.P. Density Analyser. This instrument measures the envelope volume of the lapilli by packing a
436 low-friction granular material around the clast in a reproducible way. The ratio of mass to envelope
437 volume then gave the bulk clast density, which was converted to total vesicularity using a solids
438 density of 2570 kg m^{-3} determined from shipboard measurements (see below). Each clast was then
439 placed in a Micromeritics AccuPyc II 1340 Helium Pycnometer in order to measure the volume of
440 solids plus isolated vesicles. The two datasets were merged to calculate the connected and isolated
441 vesicularities of the lapilli⁷⁵.

442

443 **Approximate hydraulic equivalence of components**

444 We carried out measurements on high-resolution (<0.1 mm) core images to test whether lithics and
445 waterlogged pumices in the Archaeos Tuff have the same settling velocities in water; i.e., are in
446 hydraulic equivalence. This was done at twelve levels of core sections 398-U1598-9H-1 and 398-
447 U1598-10H-2. In each case, we measured the diameters (mean of length and width) of the five
448 largest pumice (P) and lithic (L) clasts within a 10 cm height interval, and calculated the average
449 mean maximum diameters D_P and D_L . D_P ranged from 5 to 25 mm with a mean value of 9.6 ± 4.3 mm,
450 and D_L ranged from 1 to 6 mm with a mean value of 2.8 ± 1.2 mm.

451 Particles of gravel (>2 mm) size settle through water in the turbulent regime⁷⁶, so a
452 waterlogged pumice and a lithic particle will settle together if $(D_P \Delta \rho_P / D_L \Delta \rho_L)^{0.5} \sim 1$, assuming
453 approximate sphericity⁷⁷. Taking solids density for both (vesicular) pumices and (nonvesicular) lithics
454 as 2570 kg m^{-3} and Mediterranean seawater density as 1030 kg m^{-3} , and denoting total pumice
455 vesicularity as X_{TOT} and isolated pumice vesicularity as X_{ISO} , then we have $\Delta \rho_P \approx 2570(1 - X_{TOT}) +$
456 $1030(X_{TOT} - X_{ISO}) - 1030$ and $\Delta \rho_L = 2570 - 1030$. Taking X_{TOT} to be 0.759 and X_{ISO} to be 0.124

457 (Supplementary Table 3) gives $(D_p \Delta \rho_p / D_L \Delta \rho_L)^{0.5} = 0.77 \pm 0.13$. Given the uncertainties involved in
458 this calculation, the range of pumice vesicularities, and the non-sphericities of the particles
459 (length/width up to 3.3, with a mean value of 1.4), we take this as showing that lithics and
460 waterlogged pumices in the Archaeos Tuff at Site U1598 were in approximate hydraulic equivalence.
461

462 **Seismic data**

463 The seismic data used in this study are from three cruises between 2006 and 2019^{20,54,78}. Single-
464 channel seismic data were acquired in 2006 during the THERA project on *R/V Aegaeo*. A G-pulser was
465 used as the seismic source, with a volume of 10 in³. The general processing comprised simple
466 bandpass filtering (15-500 Hz), de-spiking, predictive deconvolution for the suppression of a strong
467 bubble signal, and spherical divergence correction. In order to migrate the data, we binned the shot
468 points into a regular spacing of 10 m. After migration, we applied a top-mute and white-noise
469 removal. The vertical resolution of these data can be approximated to 8-15 m (using the $\lambda/4$ - or $\lambda/2$ -
470 approximation).

471 For the cruise POS338 with *R/V Poseidon* in 2006, a GI-pulser was used and operated in true GI
472 mode with a primary (Generator) volume of 45 in³ and a secondary (Injector) volume of 105 in³.
473 Using a 600 m analogue streamer with 24 channels, we defined a common midpoint (CMP) spacing
474 of 12.5 m. Processing of these data comprised trace-editing, simple frequency filtering (10-500 Hz),
475 suppression of a receiver-ghost signal by predictive deconvolution, surface-related multiple
476 elimination as well as spherical divergence correction, pre-stack time migration followed by top-
477 muting and white-noise removal. These data have a main frequency of 60 Hz indicating a vertical
478 resolution of 8-15 m.

479 During the most recent cruise POS538 in 2019, we acquired seismic data with a much higher
480 lateral resolution (Common Mid-Point spacing of ~ 1.56 m). As a seismic source, we used a GI-pulser
481 that was operated in harmonic mode with primary and secondary volumes of 45 in³. Seismic energy
482 was recorded by multiple concatenated Geometrics GeoEel streamer segments, resulting in active
483 streamer sections ranging from 190 m to 250 m in length. Processing comprised trace-editing, simple
484 frequency filtering (15-1500 Hz), and multiple suppression by means of surface-related multiple
485 elimination (SRME). This was followed by spherical divergence correction, time-variant frequency
486 filtering, pre-stack time migration, top-muting, and white-noise removal. With a main frequency of
487 125 Hz, the vertical resolution is 4-8 m.

488 All processed seismic profiles were combined into an interpretation project using
489 KingdomSuite software. Here, we established the stratigraphic framework (following the
490 nomenclature in [ref 27](#) in all basins, except for the Anhydros Basin, for which we refined the
491 seismostratigraphy based on new biostratigraphic age markers), mapped seismic units, and created

492 isochron maps (vertical thickness in two-way travel time) by interpolating between the seismic
493 profiles. The Scientific colour map “batlow” is used in this study to prevent visual distortion of the
494 data and exclusion of readers with colour vision deficiencies⁷⁹.

495

496 **P-wave velocity, core-seismic integration and deposit volume estimation**

497 Integration of core data with seismic profiles requires shipboard measurement of compressional
498 wave (P-wave) velocity. This was measured *in situ* on wet samples from the working half of split
499 cores using the P-wave gantry system on the *JOIDES Resolution*. Measurements were conducted
500 perpendicular to the core using caliper transducers for every section unless core quality was
501 compromised. For more efficient contact, deionized water was applied on the lower transducer in
502 contact with the core liner. To protect the upper caliper transducer from dirt and damage, a piece of
503 plastic film was placed on the split core surface.

504 The system uses Panametrics-NDT Microscan delay line transducers, with a frequency of 500
505 kHz. The distance between the two transducers was measured with a built-in linear variable
506 differential transformer. The P-wave passing through the sample was recorded, and first arrivals
507 were picked as the initial rise of the first peak using an automated procedure. Velocities were
508 manually picked only in circumstances where the automated thresholds did not align with the
509 observed first arrival. The velocity measurement includes a correction for the core liner of known
510 thickness.

511 A total of 396 discrete P-wave velocity measurements of the Archaeos Tuff were made from
512 five sites and nine holes. The mean velocity is 1864.8 m s⁻¹ with a standard error of 0.4 m s⁻¹ and a
513 standard deviation of 168.0 m s⁻¹ (9 % of the value) We used this velocity to convert the isochron
514 maps to isochore maps (Fig. 5a) in meters and to estimate the bulk volume of the Archaeos Tuff.

515

516 **Conversion of volume to Dense Rock Equivalent (DRE)**

517 The DRE conversion factor is the volume of erupted magma and rock compared to the deposit
518 volume after removing all pore space from vesicles and intergranular voids. The conversion factor
519 can be determined by measuring water content, bulk density, grain density, and solids density from
520 samples recovered by coring using the Moisture and Density facilities on the *JOIDES Resolution*.

521 A dual balance system was used to measure both wet and dry masses. The two coupled
522 analytical balances, Mettler-Toledo XS204, were used to compensate for the ship motion; one acting
523 as a reference and the other for measurement of the unknown. Before weighing sample-standard
524 pairs, the balances were “tared” to zero based on the mean of 300 measurements; this procedure
525 was performed every 6 hours. Standard weights of similar value to the sample’s weight were placed
526 on the reference balance and the sample was placed on the balance for the unknown mass. Each

527 reported sample mass is the mean of 300 measurements. If the reference and sample masses
528 differed by more than 2 g, the measurement was aborted and then repeated after adjusting the
529 weights on the reference balance. Typically, samples were 10-20 g when wet.

530 Immediately after samples were collected, the wet sample mass was measured. Dry sample
531 mass and volume were measured after drying the samples in a convection oven for 24 hours at a
532 temperature of $105^{\circ} \pm 5^{\circ}\text{C}$ and then cooling them within a desiccator for 3 hours. Dry volume was
533 measured using a shipboard helium-displacement pycnometer with a nominal precision of $\pm 0.04 \text{ cm}^3$.
534 Each volume value consists of an average of three measurements.

535 For calculation of sediment bulk density, dry density, grain density, porosity, and void ratio, the
536 traditional ODP method is used⁸⁰ assuming a porewater salinity of 0.035 per mil and density of 1.024
537 $\text{g}\cdot\text{cm}^{-3}$. Because there are isolated vesicles entirely encased by glass in the pumice clasts, the
538 measured grain density can be lower than the density of solids. To account for isolated vesicles, we
539 use the highest measured grain density as an estimate of the solid density (2570 kg m^{-3}).

540 A total of 74 Moisture and Density samples of the Archaeos Tuff were measured from six sites
541 and nine holes. The mean DRE conversion factor is 0.341 with a standard error of 0.009. Conversion
542 of bulk to DRE volume includes any lithic components in the tuff; however this contribution accounts
543 for no more than a few percent of the volume.

544

545 **Biostratigraphic ages and palaeobathymetry**

546 Foraminifers and calcareous nannofossils were concentrated from 5-10 cm whole round sediment
547 samples; the majority of samples were taken from core catchers or the bases of cores, but where
548 appropriate additional split-core samples were taken to better define biostratigraphic datums.

549 Age assignments of studied sections were based on biostratigraphic analyses using calcareous
550 nannofossils and planktonic foraminifers. The 2020 Geologic Time Scale⁸¹ was used and updated with
551 regional biostratigraphic schemes and datums^{82,83}. The biostratigraphic datums within close
552 proximity to the Archaeos Tuff enabled the generation of age-depth models used to approximate the
553 age for the top and base of the tuff, as discussed in the main text.

554 For calcareous nannofossil analyses, standard smear slide methods were used for all samples
555 using optical adhesive as a mounting medium. The nannofossils were examined under a polarizing
556 light microscope at 1250X magnification. The taxonomic criteria of calcareous nannofossils follow
557 refs 82,84. The genera *Reticulofenestra* was placed into size categories according to ref 85. For the
558 gephyrocapsids, we adopted the concept of ref 82, and the morphological terminology used here is
559 summarized in refs 84,86. Accordingly, *Gephyrocapsa* is divided into four major groups by maximum
560 coccolith length: small *Gephyrocapsa* ($< 4 \mu\text{m}$), medium *Gephyrocapsa* (*Gephyrocapsa caribbeanica*

561 and *Gephyrocapsa oceanica*; ≥ 4 but $< 5.5 \mu\text{m}$), *Gephyrocapsa* sp. 3 (*Gephyrocapsa parallela*; ≥ 4 but
 562 $< 5.5 \mu\text{m}$) and large *Gephyrocapsa* (*G. caribbeanica* and *G. oceanica* $\geq 5.5 \mu\text{m}$).

563 The taxonomy for planktonic foraminifera follows a modified version of the phylogenetic
 564 classification of [ref 87](#), with additional species concepts based on [refs 88-90](#). Samples were prepared
 565 by manually breaking the core into small pieces and soaking in hot water when clay was present.
 566 After 5–10 minutes, samples were disaggregated and washed over a $63 \mu\text{m}$ mesh sieve to remove all
 567 mud, silt, and fine sand. The washed microfossil residue retained on the sieve was dried on filter
 568 paper in low temperature at $\sim 50^\circ\text{C}$ in a thermostatically controlled drying cabinet and subdivided
 569 with a micro-splitter into equal aliquots for examination. As a precaution against cross-
 570 contamination, sieves were cleaned with jetted water, placed in an ultrasonic bath for several
 571 minutes, dried with compressed air, and thoroughly inspected between samples.

572

573 **Table 2. Biostratigraphic datums used in this paper**

Calcareous Nannofossil events	Reference	Age (ka)
Acme Base <i>Emiliana huxleyi</i> ,	73	50
Base of <i>Emiliana huxleyi</i>	64	265
Top of <i>Pseudoemiliana lacunose</i>	64	467
Top of <i>Gephyrocapsa</i> sp.3	73	610
Top of <i>Reticulofenestra asanoi</i>	64	901
Base of <i>Gephyrocapsa</i> sp.3	73	970
Planktonic foraminifera events		
Base <i>Globigerinoides ruber</i> pink	65	330
Paracme top <i>Neogloboquadrina</i> spp. (sinistral)	65	510
Paracme base <i>Neogloboquadrina</i> spp. (sinistral)	65	910

574

575 Benthic foraminifer assemblages in the $>125 \mu\text{m}$ grain -size fraction were the primary tool used for
 576 estimating palaeowater depths. The taxonomy of benthic foraminifers is based on [refs 91-93](#).
 577 Palaeowater depth ranges were estimated using the deepest calibrated depth marker contained in
 578 each sample⁹²⁻⁹⁷. The species used (with palaeodepth ranges in brackets) are *Articulina tubulosa*
 579 (>1000 m), *Cibicides pachyderma* (200 - 700 m), *Cibicidoides mundulus* (>1000 m), *Cibicidoides*
 580 *wuellerstorfi* (>1000 m), *Gyroidina soldanii* (200 - 700 m), *Hoeglundina elegans* (50 - >700 m),
 581 *Hyalinea balthica* (200 - 700 m), *Karreriella bradyi* (200 - 700 m), *Oridorsalis umbonatus* (500 - >1000
 582 m), *Planulina ariminensis* (>50 - 700 m), *Trifarina angulosa* (50 - 700 m), *Trifarina bradyi* (200 - 700
 583 m), and *Uvigerina peregrina* (>100 - 700 m). The complex sedimentary and volcanotectonic settings
 584 sampled during IODP Expedition 398 resulted in some uncertainties in palaeowater depth
 585 reconstructions through sediment remobilization and downslope displacement of shallow-water
 586 species.

587

588

589 **References**

590
591
592
593
594
595
596
597
598
599
600
601
602
603
604
605
606
607
608
609
610
611
612
613
614
615
616
617
618
619
620
621
622
623
624
625
626
627
628
629
630
631
632
633
634
635
636
637
638
639

1. White, J.D., Schipper, C.I. & Kano, K. Submarine explosive eruptions. In: *The Encyclopedia of Volcanoes*, pp. 553-569 (Academic Press, 2015).
2. Cahalan, R.C. & Dufek, J. Explosive submarine eruptions: the role of condensable gas jets in underwater eruptions. *J. Geophys. Res. Solid Earth* **126**, p.e2020JB020969 (2021).
3. Hajimirza, S., Jones, T.J., Moreland, W.M., Gonnermann, H.M. & Thordarson, T. Quantifying the water-to-melt mass ratio and its impact on eruption plumes during explosive hydromagmatic eruptions. *Geochem. Geophys. Geosys.* **23**, p.e2021GC010160 (2022).
4. Rowell, C.R., Jellinek, A.M., Hajimirza, S. & Aubry, T.J. External surface water influence on explosive eruption dynamics, with implications for stratospheric sulfur delivery and volcano-climate feedback. *Frontiers in Earth Science*, **10**, 788294 (2022).
5. Gilchrist, J.T., Jellinek, A.M., Hooft, E.E. & Wanket, S. Submarine terraced deposits linked to periodic collapse of caldera-forming eruption columns. *Nat. Geosci.* **16**, 446-453 (2023).
6. Fiske, R.S., Naka, J., Iizasa, K., Yuasa, M. & Klaus, A. Submarine silicic caldera at the front of the Izu-Bonin arc, Japan: Voluminous seafloor eruptions of rhyolite pumice. *Geol. Soc. Am. Bull.* **113**, 813-824 (2001).
7. Rotella, M.D., Wilson, C.J., Barker, S.J., Schipper, C.I., Wright, I.C. & Wysoczanski, R.J. Dynamics of deep submarine silicic explosive eruptions in the Kermadec arc, as reflected in pumice vesicularity textures. *J. Volcanol. Geotherm. Res.* **301**, 314-332 (2015).
8. Proud, S.R., Prata, A.T. & Schmauß, S. The January 2022 eruption of Hunga Tonga-Hunga Ha'apai Volcano reached the mesosphere. *Science*, **378**, 554-557 (2022).
9. Seabrook, S. et al. Pyroclastic density currents explain far-reaching and diverse seafloor impacts of the 2022 Hunga Tonga Hunga Ha'apai eruption. Preprint at *Research Square* <https://doi.org/10.21203/rs.3.rs-2395332/v1> (2023).
10. Clare, M.A. et al. Fast and destructive density currents created by ocean-entering volcanic eruptions, *Science* **381**, 1085–1092 (2023)
11. Cas, R.A. & Wright, J.V. Subaqueous pyroclastic flows and ignimbrites: an assessment. *Bull. Volcanol.* **53**, 357-380 (1991).
12. Kano, K., Yamamoto, T. & Ono, K. Subaqueous eruption and emplacement of the Shinjima Pumice, Shinjima (Moeshima) Island, Kagoshima Bay, SW Japan. *J. Volcanol. Geotherm. Res.* **71**, 187-206 (1996).
13. Allen, S.R. & McPhie, J. Products of Neptunian eruptions. *Geology* **37**, 639-642 (2009).
14. Jutzeler, M., McPhie, J. & Allen, S.R. Submarine eruption-fed and resedimented pumice-rich facies: the Dogashima Formation (Izu Peninsula, Japan). *Bull. Volcanol.* **76**, 1-29 (2014).
15. Nomikou, P., Papanikolaou, D., Alexandri, M., Sakellariou, D. & Rousakis, G. Submarine volcanoes along the Aegean volcanic arc. *Tectonophysics*. **597**, 123-146 (2013).
16. Nomikou P., Hübscher C., & Carey S. The Christiana–Santorini–Kolumbo Volcanic Field. *Elements* **15**, 171–176 (2019).
17. Druitt, T.H., Edwards, L., Mellors, R.M., Pyle, D.M., Sparks, R.S.J., Lanphere, M., Davies, M. & Barreiro, B. Santorini Volcano. *Geol. Soc. London Memoir* **19**, 165pp (1999).
18. Gertisser, R., Preece, K. & Keller, J. The Plinian Lower Pumice 2 eruption, Santorini, Greece: magma evolution and volatile behaviour. *J. Volcanol. Geotherm. Res.* **186**, 387-406 (2009).
19. Kutterolf, S., Freundt, A., Druitt, T.H., McPhie, J., Nomikou, P., Pank, K., Schindlbeck-Belo, J.C., Hansteen, T.H. & Allen, S.R. The medial offshore record of explosive volcanism along the central to eastern Aegean Volcanic Arc: 2. Tephra ages and volumes, eruption magnitudes and marine sedimentation rate variations. *Geochem. Geophys. Geosys.* **22**, p.e2021GC010011 (2021).
20. Hübscher, C., Ruhnau, M. & Nomikou, P. Volcano-tectonic evolution of the polygenetic Kolumbo submarine volcano/Santorini (Aegean Sea). *J. Volcanol. Geotherm. Res.* **291**, 101-111 (2015).

- 640 21. Nomikou, P., Hübscher, C., Ruhнау, M. & Bejelou, K. Tectono-stratigraphic evolution through
641 successive extensional events of the Anydros Basin, hosting Kolumbo volcanic field at the
642 Aegean Sea, Greece. *Tectonophys.* **671**, 202-217 (2016).
- 643 22. Nomikou, P., Hübscher, C., Papanikolaou, D., Farangitakis, G.P., Ruhнау, M. & Lampridou, D.
644 Expanding extension, subsidence and lateral segmentation within the Santorini - Amorgos
645 basins during Quaternary: implications for the 1956 Amorgos events, central-south Aegean
646 Sea, Greece. *Tectonophys.* **722**, 138–153 (2018).
- 647 23. Preine, J., Karstens, J., Hübscher, C., Nomikou, P., Schmid, F., Crutchley, G.J., Druitt, T.H. &
648 Papanikolaou, D. Spatio-temporal evolution of the Christiana-Santorini-Kolumbo volcanic
649 field, Aegean Sea. *Geology*, **50**, 96–100 (2021).
- 650 24. Hooft, E.E.E., Nomikou, P., Toomey, D.R., Lampridou, D., Getz, C., Christopoulou, M.-E.,
651 O’Hara, D., Arnoux, G.M., Bodmer, M., Gray, M., Heath, B.A., & VanderBeek, B.P. Backarc
652 tectonism, volcanism, and mass wasting shape seafloor morphology in the Santorini-
653 Christiana-Amorgos region of the Hellenic Volcanic Arc. *Tectonophys.* **712–713**, 396–414
654 (2017).
- 655 25. Tsampouraki-Kraounaki, K. & Sakellariou, D. Seismic stratigraphy and geodynamic evolution
656 of Christiana Basin, South Aegean Arc. *Marine Geol.* **399**, 135–147 (2018).
- 657 26. Heath, B.A., Hooft, E.E.E., Toomey, D.R., Papazachos, C.B., Nomikou, P., Paulatto, M.,
658 Morgan, J.V. & Warner, M.R. Tectonism and its relation to magmatism around Santorini
659 Volcano from upper crustal P wave velocity. *J. Geophys. Res. Solid Earth* **124**, 10610-10629
660 (2019).
- 661 27. Preine, J., Karstens, J., Hübscher, C., Crutchley, G.J., Druitt, T.H., Schmid, F. & Nomikou, P. The
662 Hidden Giant: How a rift pulse triggered a cascade of sector collapses and voluminous
663 secondary mass-transport events in the early evolution of Santorini. *Basin Res.* **34**, 1465–
664 1485 (2022).
- 665 28. Francalanci, L. & Zellmer, G.F. Magma genesis at the South Aegean volcanic arc. *Elements*,
666 **15**, 65-170 (2019).
- 667 29. Cantner, K., Carey, S. & Nomikou, P. Integrated volcanologic and petrologic analysis of the
668 1650 AD eruption of Kolumbo submarine volcano, Greece. *J. Volcanol. Geotherm. Res.* **269**,
669 28–43 (2014).
- 670 30. Fuller, S., Carey, S. & Nomikou, P. Distribution of fine-grained tephra from the 1650 CE
671 submarine eruption of Kolumbo Volcano, Greece. *J. Volcanol. Geotherm. Res.* **352**, 10-25
672 (2018).
- 673 31. Parks, M.M., Moore, J.D., Papanikolaou, X., Biggs, J., Mather, T.A., Pyle, D.M., Raptakis, C.,
674 Paradissis, D., Hooper, A., Parsons, B. & Nomikou, P. From quiescence to unrest: 20 years of
675 satellite geodetic measurements at Santorini volcano, Greece. *J. Geophys. Res. Solid Earth*
676 **120**, 1309-1328 (2015).
- 677 32. McVey, B.G., Hooft, E.E.E., Heath, B.A., Toomey, D.R., Paulatto, M., Morgan, J.V., Nomikou, P.
678 & Papazachos, C.B.,. Magma accumulation beneath Santorini volcano, Greece, from P-wave
679 tomography. *Geology*, **48**, 231-235 (2020).
- 680 33. Chrapkiewicz, K. et al. Magma Chamber Detected Beneath an Arc Volcano With Full-
681 Waveform Inversion of Active-Source Seismic Data. *Geochem. Geophys. Geosys.* **23**,
682 p.e2022GC010475 (2022).
- 683 34. Jutzeler, M., White, J.D.L., Talling, P.J., McCanta, M., Morgan, S., Le Friant, A. & Ishizuka, O.
684 Coring disturbances in IODP piston cores with implications for offshore record of volcanic
685 events and the Missoula megafloods. *Geochem. Geophys. Geosys.* **15**, 3572–3590 (2014).
- 686 35. Inman, D.L. Measures for describing the size distribution of sediments. *J. Sediment. Res.* **22**,
687 125-145 (1952).
- 688 36. Walker, G.P.L. Ignimbrite types and ignimbrite problems. *J. Volcanol. Geotherm. Res.* **17**, 65-
689 88 (1983).
- 690 37. Spratt, R.M. & Lisiecki, L.E. A Late Pleistocene sea level stack, *Climate of the Past* **12**, 1079–
691 1092 (2016).

- 692 38. Papoulia, C. Late Pleistocene to Early Holocene sea-crossings in the Aegean: direct, indirect
693 and controversial evidence. *Géoarchéologie des Îles de Méditerranée*. CNRS Editions, Paris,
694 **33**, 46 (2016).
- 695 39. Keller, J., Dietrich, V., Reusser, E., Gertisser, R. & Aarburg, S. Recognition of a major
696 ignimbrite in the early evolution of the Santorini Group: the Christiani Ignimbrite. *Cities on*
697 *Volcanoes 6, Tenerife, Spain* pp. 4–5 (Abstract) (2010). [https://www.earth-](https://www.earth-prints.org/bitstream/2122/6924/1/Cities%20on%20Volcanoes%206%20Abstracts%20Volume.pdf)
698 [prints.org/bitstream/2122/6924/1/Cities%20on%20Volcanoes%206%20Abstracts%20Volume](https://www.earth-prints.org/bitstream/2122/6924/1/Cities%20on%20Volcanoes%206%20Abstracts%20Volume.pdf)
699 [.pdf](https://www.earth-prints.org/bitstream/2122/6924/1/Cities%20on%20Volcanoes%206%20Abstracts%20Volume.pdf)
- 700 40. Keller, J., Gertisser, R., Reusser, E. & Dietrich, V. Pumice deposits of the Santorini Lower
701 Pumice 2 eruption on Anafi island, Greece: Indications for a Plinian event of exceptional
702 magnitude. *J. Volcanol. Geotherm. Res.* **278**, 120-128 (2014).
- 703 41. Cashman, K.V. & Fiske, R.S. Fallout of pyroclastic debris from submarine volcanic eruptions.
704 *Science*, **253**, 275-280 (1991).
- 705 42. Allen, S.R., Freundt, A. & Kurokawa, K. Characteristics of submarine pumice-rich density
706 current deposits sourced from turbulent mixing of subaerial pyroclastic flows at the
707 shoreline: Field and experimental assessment. *Bull. Volcanol.* **74**, 657-675 (2012).
- 708 43. Cole, R.B. & Decelles, P.G. Subaerial to submarine transitions in early Miocene pyroclastic
709 flow deposits, southern San Joaquin basin, California. *Geol. Soc. Am. Bull.* **103**, 221-235
710 (1991).
- 711 44. Jutzeler, M., Manga, M., White, J.D.L., Talling, P.J., Proussevitch, A.A., Watt, S.F.L., Cassidy,
712 M., Taylor, R.N., Le Friant, A. & Ishizuka, O. Submarine deposits from pumiceous pyroclastic
713 density currents traveling over water: An outstanding example from offshore Montserrat
714 (IODP 340). *Geol. Soc. Am. Bull.* **129**, 392-414 (2017).
- 715 45. Kutterolf, S., Schindlbeck, J.C., Scudder, R.P., Murray, R.W., Pickering, K.T., Freundt, A.,
716 Labanieh, S., Heydolph, K., Saito, S., Naruse, H. & Underwood, M.B. Large volume submarine
717 ignimbrites in the Shikoku Basin: An example for explosive volcanism in the Western Pacific
718 during the Late Miocene. *Geochem. Geophys. Geosys.* **15**, 1837-1851 (2014).
- 719 46. Trofimovs, J., Amy, L., Boudon, G., Deplus, C., Doyle, E., Fournier, N., Hart, M.B., Komorowski,
720 J.C., Le Friant, A., Lock, E.J. & Pudsey, C. Submarine pyroclastic deposits formed at the
721 Soufrière Hills volcano, Montserrat (1995–2003): What happens when pyroclastic flows enter
722 the ocean?. *Geology* **34**, 549-552 (2006).
- 723 47. Freundt, A. Entrance of hot pyroclastic flows into the sea: experimental observations. *Bull.*
724 *Volcanol.* **65**, 144-164 (2003).
- 725 48. Mandeville, C.W., Carey, S., Sigurdsson, H. & King, J. Paleomagnetic evidence for high-
726 temperature emplacement of the 1883 subaqueous pyroclastic flows from Krakatau Volcano,
727 Indonesia. *J. Geophys. Res. Solid Earth* **99**, 9487-9504 (1994).
- 728 49. Freundt, A., Schindlbeck-Belo, J.C., Kutterolf, S. & Hopkins, J.L. Tephra layers in the marine
729 environment: a review of properties and emplacement processes. *Geol. Soc. Lond. Spec.*
730 *Publ.* **520** 595-637 (2023).
- 731 50. Bryan, S.E., Cook, A.G., Evans, J.P., Hebden, K., Hurrey, L., Colls, P., Jell, J.S., Weatherley, D. &
732 Firn, J. Rapid, long-distance dispersal by pumice rafting. *PLoS ONE* **7**, p.e40583 (2012).
- 733 51. Mitchell, S.J., Fauria, K.E., Houghton, B.F. & Carey, R.J. Sink or float: microtextural controls on
734 the fate of pumice deposition during the 2012 submarine Havre eruption. *Bull. Volcanol.* **83**,
735 1-20 (2021).
- 736 52. Whitham, A.G. & Sparks, R.S.J. Pumice. *Bull. Volcanol.* **48**, 209-223 (1986).
- 737 53. Fauria, K.E., Manga, M. & Wei, Z. Trapped bubbles keep pumice afloat and gas diffusion
738 makes pumice sink. *Earth Planet. Sci. Lett.* **460**, 50-59 (2017).
- 739 54. Karstens, J. et al. Revised Minoan eruption volume as benchmark for large volcanic eruptions.
740 *Nat. Commun.* **14**:2497 (2023).
- 741 55. Roche, O., Azzaoui, N. & Guillin, A. Discharge rate of explosive volcanic eruption controls
742 runout distance of pyroclastic density currents. *Earth Planet. Sci. Lett.* **568**, 117017 (2021).

- 743 56. Carey, S., Sigurdsson, H., Mandeville, C. & Bronto, S. Pyroclastic flows and surges over water:
744 an example from the 1883 Krakatau eruption. *Bull. Volcanol.* **57**, 493-511 (1996).
- 745 57. Allen, S.R. & Cas, R.A. Transport of pyroclastic flows across the sea during the explosive,
746 rhyolitic eruption of the Kos Plateau Tuff, Greece. *Bull. Volcanol.* **62**, 441-456 (2001).
- 747 58. Dufek, J. & Bergantz, G.W. Dynamics and deposits generated by the Kos Plateau Tuff
748 eruption: Controls of basal particle loss on pyroclastic flow transport. *Geochem. Geophys.*
749 *Geosys.* **8**, 12 (2007).
- 750 59. Dufek, J., Wexler, J. & Manga, M. Transport capacity of pyroclastic density currents:
751 Experiments and models of substrate-flow interaction, *J. Geophys. Res.* **114**, B11203 (2009).
- 752 60. Valentine, G. A. Stratified flow in pyroclastic surges. *Bull. Volcanol.* **49**, 616–630 (1987).
- 753 61. Breard, E.C., Lube, G., Jones, J.R., Dufek, J., Cronin, S.J., Valentine, G.A. & Moebis, A. Coupling
754 of turbulent and non-turbulent flow regimes within pyroclastic density currents. *Nature*
755 *Geosci.* **9**, 767–771 (2016).
- 756 62. Lucchi, F., Sulpizio, R., Meschiari, S., Tranne, C.A., Albert, P.G., Mele, D. and Dellino, P.
757 Sedimentological analysis of ash-rich pyroclastic density currents, with special emphasis on
758 sin-depositional erosion and clast incorporation: The Brown Tuff eruptions (Vulcano, Italy).
759 *Sed. Geol.* **427**, p.106040 (2022).
- 760 63. Wilson, C.J.N. Ignimbrite morphology and the effects of erosion: a New Zealand case study.
761 *Bull. Volcanol.* **53**, 635-644 (1991).
- 762 64. Silleni, A., Giordano, G., Isaia, R. & Ort, M.H. The magnitude of the 39.8 ka Campanian
763 Ignimbrite eruption, Italy: Method, uncertainties and errors. *Frontiers in Earth Science* **8**,
764 p.543399 (2020).
- 765 65. Folkes, C.B., Wright, H.M., Cas, R.A., de Silva, S.L., Lesti, C. & Viramonte, J.G. A re-appraisal of
766 the stratigraphy and volcanology of the Cerro Galán volcanic system, NW Argentina. *Bull.*
767 *Volcanol.* **73**, 1427-1454 (2011).
- 768 66. Cook, G.W., Wolff, J.A. & Self, S. Estimating the eruptive volume of a large pyroclastic body:
769 the Otowi Member of the Bandelier Tuff, Valles caldera, New Mexico. *Bull. Volcanol.* **78**, 1-11
770 (2016).
- 771 67. Vakhrameeva, P., Koutsodendris, A., Wulf, S., Fletcher, W.J., Appelt, O., Knipping, M.,
772 Gertisser, R., Trieloff, M. & Pross, J. The cryptotephra record of the Marine Isotope Stage 12
773 to 10 interval (460–335 ka) at Tenaghi Philippon, Greece: Exploring chronological markers for
774 the Middle Pleistocene of the Mediterranean region. *Quat. Sci. Rev.* **200**, 313-333 (2018).
- 775 68. Allen, S.R., Stadlbauer, E. & Keller, J. Stratigraphy of the Kos Plateau Tuff: Product of a major
776 Quaternary explosive rhyolitic eruption in the eastern Aegean, Greece. *Int. J. Earth Sci.* **88**,
777 132-156 (1999).
- 778 69. Fisher, R.V., & Schmincke, H.-U. *Pyroclastic Rocks*. Springer-Verlag, 472pp (1984).
- 779 70. Nomikou, P., Carey, S., Papanikolaou, D., Croff Bell, K., Sakellariou, D., Alexandri, M., &
780 Bejelou, K. Submarine volcanoes of the Kolumbo volcanic zone NE of Santorini caldera,
781 Greece. *Global and Planetary Change*, **90–91**, 135–151 (2012).
- 782 71. Puchelt, H., Murad, E. & Hubberten, H.W. Geochemical and petrological studies of lavas,
783 pyroclastica and associated xenoliths from the Christiana Islands, Aegean Sea. *Neues*
784 *Jahrbuch Für Mineralogie-Abhandlungen*, **131**, 140-155 (1977).
- 785 72. Aarburg, S. & Frechen, M. Die pyroklastischen Abfolgen der Christiana-Inseln (Süd-Ägäis,
786 Griechenland). In Becker-Haumann, R. & Frechen, M. (eds.) *Terrestrische Quartargeologie*
787 260–276 (1999).
- 788 73. Hunt, J.B. & Hill, P.G. Tephrological implications of beam size—sample-size effects in electron
789 microprobe analysis of glass shards. *J. Quat. Sci.* **16**, 105-117 (2001).
- 790 74. Jarosewich, E., Nelen, J.A. & Norberg, J.A. Reference samples for electron microprobe
791 analysis. *Geostandards Newsletter* **4**, 43-47 (1980).
- 792 75. Formenti, Y. & Druitt, T.H. Vesicle connectivity in pyroclasts and implications for the
793 fluidisation of fountain-collapse pyroclastic flows, Montserrat (West Indies). *Earth Planet. Sci.*
794 *Lett.* **214**, 561-574 (2003).

- 795 76. McCave, I.N. Deposition from suspension. In: Seller, R. C., Cocks, R. & Plimer, R. (eds).
796 *Encyclopedia of Geology*, **5**, 8-17, Elsevier (2005).
- 797 77. Burgisser, A. & Gardner, J.E. Using hydraulic equivalences to discriminate transport processes
798 of volcanic flows. *Geology*, **34**, 57-160 (2006).
- 799 78. Sigurdsson, H., Carey, S., Alexandri, M., Vougioukalakis, G., Croff, K., Roman, C., Sakellariou,
800 D., Anagnostou, C., Rousakis, G., Ioakim, C. & Goguo, A. Marine investigations of Greece's
801 Santorini volcanic field. *Eos, Trans. Am. Geophys. Union* **87**, 337-342 (2006).
- 802 79. Crameri, F. *Scientific colour maps*. Zenodo (2018). <http://doi.org/10.5281/zenodo.1243862>
- 803 80. Blum, P. Technical Note 26: Physical Properties Handbook—A Guide to the Shipboard
804 Measurement of Physical Properties of Deep-Sea Cores. *Ocean Drilling Program* (1997)
805 <http://www-odp.tamu.edu/publications/tnotes/tn26/INDEX.HTM>
- 806 81. Raffi, I., Wade, B.S. & Pälke, H. The Neogene Period. In: Gradstein, F.M., Ogg, J.G., Schmitz,
807 M.D. & Ogg, G.M. (eds), *Geological Time Scale 2020*, pp 1141-1200 (Elsevier, 2020).
- 808 82. Raffi, I., Backman, J., Fornaciari, E., Pälke, H., Rio, D., Lourens, L. & Hilgen, F. A review of
809 calcareous nannofossil astrobiochronology encompassing the past 25 million years. *Quat. Sci.*
810 *Rev.* **25**, 3113–3137 (2006).
- 811 83. Lirer, F., Foresi, L.M., Laccarino, S.M., Salvatorini, G., Turco, E., Cosentino, C., Siervo, F.J. &
812 Caruso, A. Mediterranean Neogene planktonic foraminifer biozonation and biochronology.
813 *Earth Sci. Rev.* **196**, 102869 (2019).
- 814 84. Perch-Nielsen, K. Cenozoic calcareous nannofossils. In: Bolli, H.M., Saunders, J.B., Perch-
815 Nielsen, K. (eds.), *Plankton Stratigraphy*, pp427–554 (Cambridge University Press, 1985).
- 816 85. Young, J.R. Neogene. In: Bown, P.R. (ed), *Calcareous Nannofossil Biostratigraphy* pp. 225-265
817 (Kluwer Academic Publishing, 1999).
- 818 86. Takayama, T. & Sato, T. Coccolith biostratigraphy of the north Atlantic Ocean, Deep Sea
819 Drilling Project Leg 94. In: Ruddiman, W.F., Kidd, R.B., Thomas, E. et al. (eds), *Initial Reports*
820 *DSDP 94*, 651- 702. (U.S. Govt. Printing Office, 1987).
- 821 87. Kennett, J.P. & Srinivasan, M.S. Neogene planktonic foraminifera. *A phylogenetic atlas* **265**,
822 546-548 (1983).
- 823 88. Huber, B.T., Petrizzo, M.R., Young, J.R., Falzoni, F., Gilardoni, S.E., Bown, P.R. & Wade, B.S.
824 Pforams@ microtax. *Micropaleontology*, **62**, 429-438 (2016).
- 825 89. Schiebel, R. & Hemleben, C. *Planktonic Foraminifers in the Modern Ocean 2020*, pp1–358
826 (Springer-Verlag, 2017).
- 827 90. Lam, A.R. & Leckie, R.M. Late Neogene and Quaternary diversity and taxonomy of subtropical
828 to temperate planktic foraminifera across the Kuroshio Current Extension, northwest Pacific
829 Ocean. *Micropaleontology* **66**: 177-268 (2020).
- 830 91. Cimerman, F. & Langer, M. Mediterranean Foraminifera. *Academia Scientiarum et Artium*
831 *Slovenica Classis IV* **30** (1991). Cimerman, F., 1991.
- 832 92. Sgarella, F. & Moncharmont Zei, M. Benthic foraminifera in the Gulf of Naples (Italy):
833 systematics and autoecology. *Bollettino della Societa Paleontologica Italiana*, **32**, 145-264
834 (1993).
- 835 93. Rasmussen, T.L. & Thomsen, E. Foraminifera and paleoenvironment of the Plio-Pleistocene
836 Kallithea Bay section, Rhodes, Greece: evidence for cyclic sedimentation and shallow-water
837 sapropels. *Cushman Foundation for Foraminiferal Research, Spec. Publ.* **39**, 15-51 (2005).
- 838 94. Wright, R. Neogene paleobathymetry of the Mediterranean based on benthic Foraminifers
839 from DSDP Leg 42A. In: Hsu, K.L. & Montadert, L. (eds). *Initial Rep Deep Sea Drill Proj. XLII:*
840 *Scripps Inst. Oceanog.* 837-846 (1975).
- 841 95. De Stigter, H.C., Jorissen, F.J. & Van der Zwaan, G.J. Bathymetric distribution and
842 microhabitat partitioning of live (Rose Bengal stained) benthic foraminifera along a shelf to
843 bathyal transect in the southern Adriatic Sea. *J. Foram. Res.* **28**, 40-65 (1998).
- 844 96. De Rijk, S., Troelstra, S.R. & Rohling, E.J. Benthic foraminiferal distribution in the
845 Mediterranean Sea. *J. Foram. Res.* **29**, 93-103 (1999).

846 97. Milker, Y., Weinkauf, M.F.G., Titschack, J., Freiwald, A., Krüger, S., Jorissen, F.J., & Schmiedl,
847 G. Testing the applicability of a benthic foraminiferal-based transfer function for the
848 reconstruction of paleowater depth changes in Rhodes (Greece) during the early Pleistocene.
849 *PLoS ONE*, **12**, e0188447 (2017).

850

851

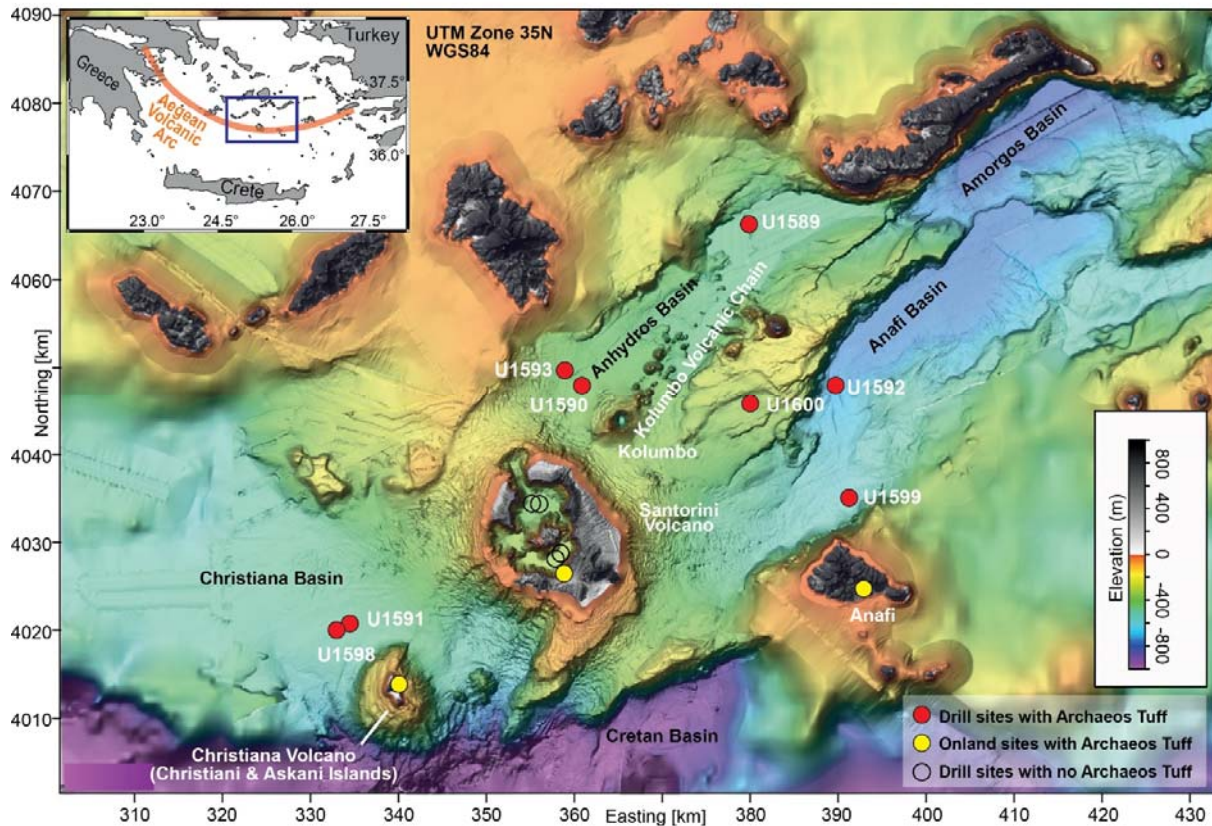
852 **Acknowledgements**

853

854 This research used samples and data provided by the International Ocean Discovery
855 Program (IODP). We thank the technical staff of the *JOIDES Resolution* for their efforts in attaining
856 the scientific goals of Expedition 398, and all of the shipboard personnel for a great experience.
857 Special gratitude goes to Bill Rheinehart, Chieh Peng and colleagues in helping us overcome many
858 obstacles and to Katerina Petronotis and the leadership of IODP for their support. We thank the
859 member organizations of IODP for financial aid and the Municipality of Thera for help in preparing for
860 the expedition. This is Laboratory of Excellence ClerVolc contribution XXX.

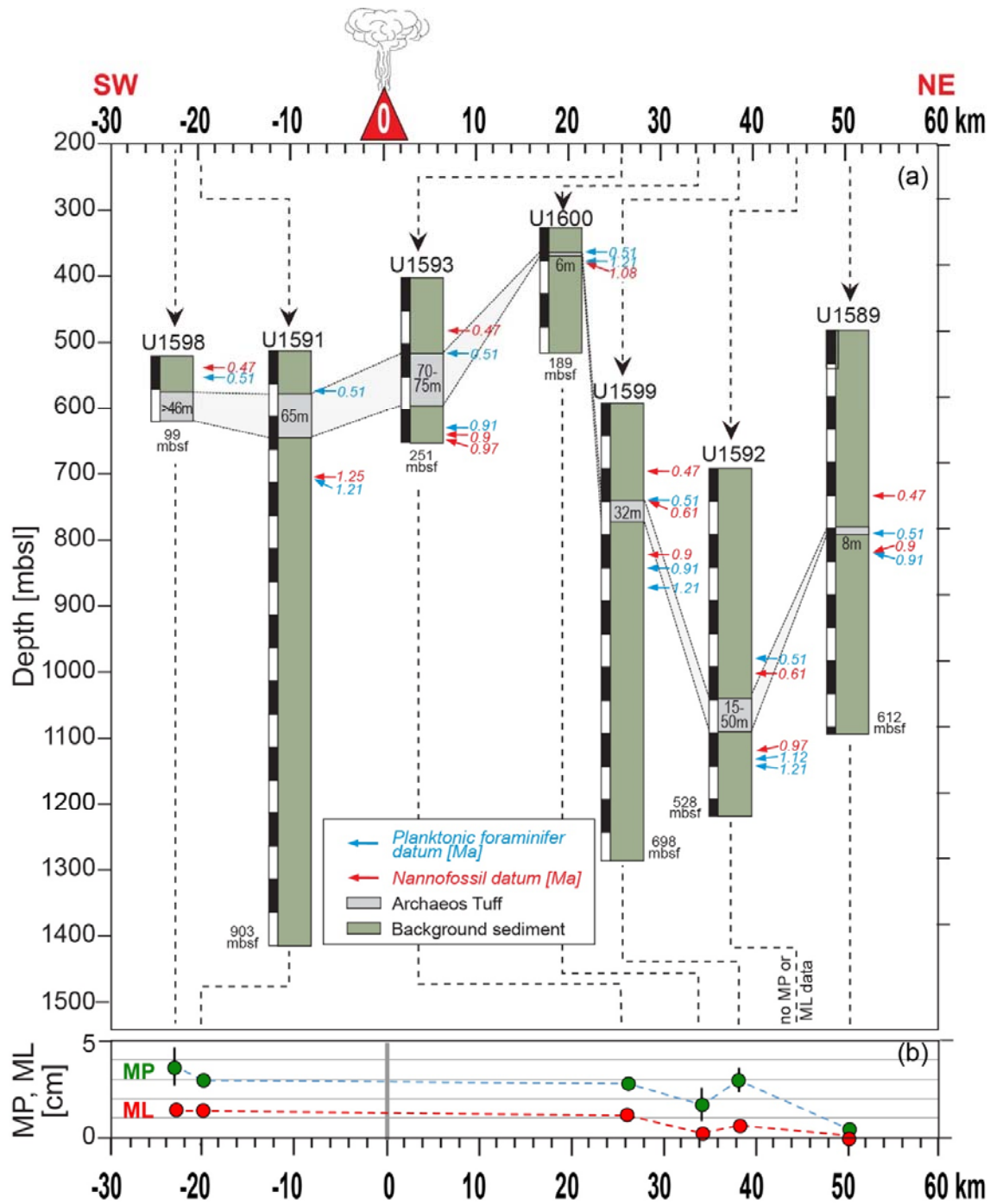
861

862

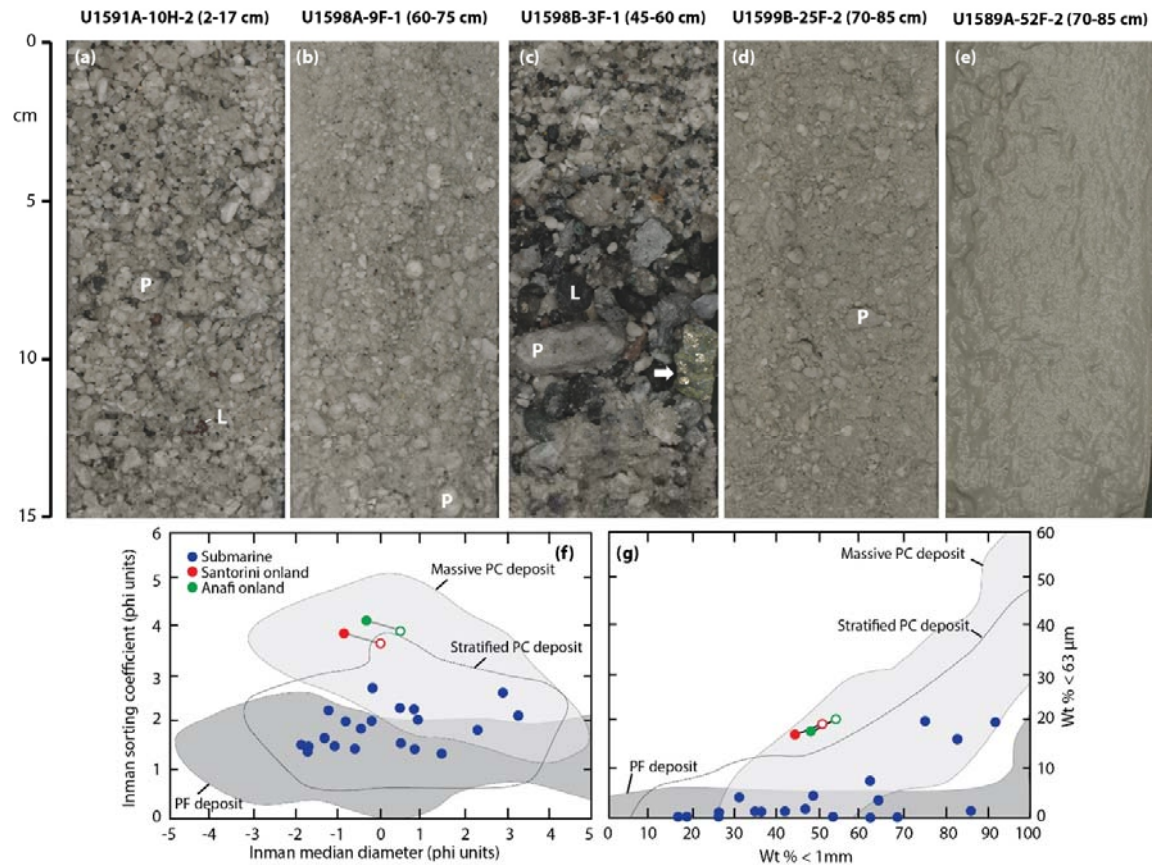


863
 864
 865
 866
 867
 868
 869

Figure 1. Occurrences of the Archaeos Tuff at the IODP drill sites (red dots) and onland sites (yellow dots). The drill sites are labelled with their IODP site numbers. No Archaeos Tuff was in fact recovered at Site U1590, but its presence is seen on seismic profiles. The inset shows the location on the South Aegean Volcanic Arc. See Methods for sources of bathymetric data.

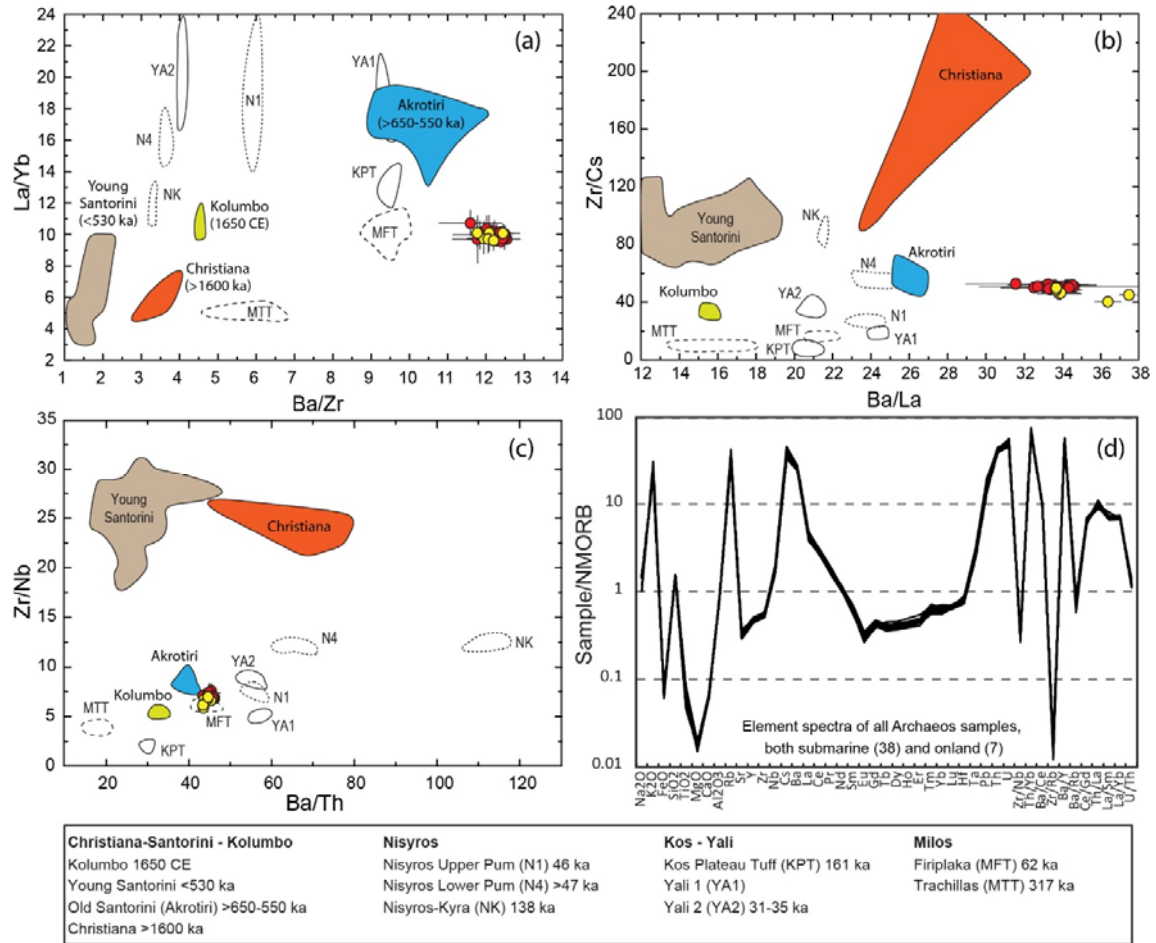


870 **Figure 2.** (a) Biostratigraphic constraints on the age of the Archaeos Tuff indicating its thicknesses
 871 and depth of at the drilled sites. Bathymetric depths of the drill sites are shown with distance from
 872 the suspected source. mbsl: metres below sea level. mbsf: metres below sea floor. Ma: million years.
 873 Zero distance is arbitrarily taken as the end of the Akrotiri Peninsula on Santorini. (b) Maximum
 874 pumice (MP) and maximum lithic (ML) diameters at each site, being the average of the five largest
 875 clasts observed on high-resolution core images at each site.
 876



878

879 **Figure 3.** (a-e) Submarine facies of the Archaeos Tuff. Panel c shows a lithic-rich segregation layer. P:
 880 pumice clast. L: Lithic clast. Arrow marks a greenschist clast rich in epidote and pyrite. (f-g) Grain size
 881 size characteristics of the Archaeos Tuff in core samples judged to be little affected by core disturbance
 882 effects³⁴. Two analyses are shown for each onland sample: total sample (dot) and <8 mm size fraction
 883 (circle), the latter for comparison with the core samples. The Inman grain size parameters are taken
 884 from [ref 35](#). The fields for pyroclastic current (PC) and pyroclastic fall (PF) are taken from [ref 36](#).
 885
 886



888

889

890

891

892

893

894

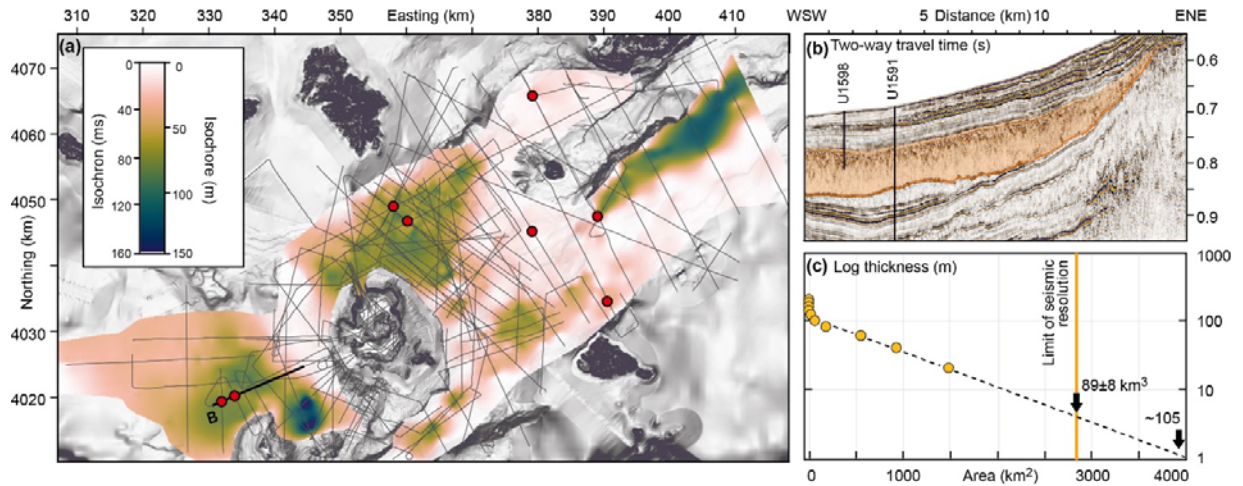
895

896

897

898

Figure 4. (a-c) Incompatible trace element ratio plots showing the compositional similarity of the onland (yellow dots) and offshore (red dots) samples of the Archaeos Tuff to those of the Early Centres of Akrotiri (>650-550 ka), and the differences with other volcanic centres of the South Aegean Volcanic Arc and the younger tuffs of Santorini (<530 ka). All the analyses are glasses (data of ref. 19), apart from Christiana, which are the authors' unpublished analyses of whole-rock lavas with >60 % SiO₂. (d) Element spectra normalized to N-MORB for 38 offshore samples (at seven drill sites shown in red in Fig. 1) and 7 onshore samples (yellow locations in Fig. 1) of the Archaeos Tuff, showing the essentially identical compositions.



899
 900
 901
 902
 903
 904
 905
 906
 907
 908
 909
 910

Figure 5. (a) Combined two-way travel (TWT) time and thickness map of the Archaeos Tuff, derived by integration of the drill core stratigraphy with seismic profiles, and conversion to thickness using onboard measurements of P-wave velocity. Red dots are the drill sites. (b) WSW-ENE seismic profile across the Christiana Basin (bold line), showing the Archaeos Tuff in orange. The orange line marks the base of the deposit, which is erosional on the underlying strata in this part of the basin. (c) Plot of log(thickness) versus cumulative area from (a). Integrating within the boundary on (a) gives a volume of $89 \pm 8 \text{ km}^3$. Extrapolating to 1 m on the plot gives $\sim 105 \text{ km}^3$. This extrapolation is based on the known linearity of data on this plot for several subaerial ignimbrites^{63,64}.